

Antimony arsenide: Chemical ordering in the compound SbAs

Daniel P. Shoemaker,¹ Thomas C. Chasapis,² Dat Do,³ Melanie C. Francisco,¹ Duck Young Chung,¹ S. D. Mahanti,³ Anna Llobet,⁴ and Mercouri G. Kanatzidis^{1,*}

¹Materials Science Division, Argonne National Laboratory, Argonne, IL 60439, USA

²Department of Chemistry, Northwestern University, Evanston, Illinois 60208, United States

³Department of Physics and Astronomy, Michigan State University, East Lansing, Michigan 48824, USA

⁴Lujan Neutron Scattering Center, Los Alamos National Laboratory, Los Alamos, NM 87545, USA

The semimetallic Group V elements display a wealth of correlated electron phenomena due to a small indirect band overlap that leads to relatively small, but equal, numbers of holes and electrons at the Fermi energy with high mobility. Their electronic bonding characteristics produce a unique crystal structure, the rhombohedral A7 structure, which accommodates lone pairs on each site. Here we show that the A7 structure can display chemical ordering of Sb and As, which were previously thought to mix randomly. Our structural characterization of the compound SbAs is performed by single-crystal and high-resolution synchrotron x-ray diffraction, and neutron and x-ray pair distribution function analysis. All least-squares refinements indicate ordering of Sb and As, resulting in a GeTe-type structure without inversion symmetry. High-temperature diffraction studies reveal an ordering transition around 550 K. Transport and infrared reflectivity measurements, along with first-principles calculations, confirm that SbAs is a semimetal, albeit with a direct band separation larger than that of Sb or As. Because even subtle substitutions in the semimetals, notably $\text{Bi}_{1-x}\text{Sb}_x$, can open semiconducting energy gaps, a further investigation of the interplay between chemical ordering and electronic structure on the A7 lattice is warranted.

PACS numbers: 71.20.Gj 81.05.Bx 72.15.Jf

I. INTRODUCTION

The Group V elements As, Sb, and Bi have a structure all their own, unshared by any other elements. This “A7” crystal structure in Figure 1(a) is a consequence of the unique electronic structure of these elements, where s - p hybridization leads to formation of a lone pair.^{1,2} As a result, the A7 structure has rhombohedral crystal symmetry and lies in space group $R\bar{3}m$. It is only a small distortion removed from simple cubic symmetry, which can be experimentally accessed under applied pressure.³⁻⁵ The band structure that drives formation of the A7 phase also causes these elements to be the prototypical semimetals, with a small offset band overlap, small number of carriers compared to typical metals (10^{-5} as many), high mobility, and nearly equal concentrations of electron and hole carriers.⁶

Their unique electronic properties have made the semimetals a fascinating arena in condensed matter physics, permitting initial measurements of the quantum mechanical oscillatory Shubnikov-de Haas and de Haas van Alphen effects, Seebeck’s discovery of the thermoelectric effect, and Hall’s measurements of spin-dependent transport.⁷ Because the band overlap in semimetals is so delicate, they are tunable by doping for thermoelectric applications⁸ and in topological insulators.⁹

Alloying the Group V elements themselves can produce unexpected results. The $\text{Bi}_{1-x}\text{Sb}_x$ solid solution is semimetallic on both ends but becomes semiconducting for $0.07 < x < 0.22$ by opening a gap at the L point and removing overlap at the T point of the Brillouin zone.^{10,11} Bi and As are not chemically miscible.¹² Previ-

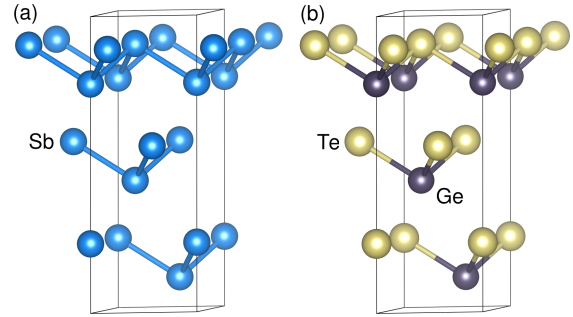


FIG. 1. (Color online) Unit cell of the A7 structure (a) of pure As, Sb, and Bi (and black P at high pressure) with $R\bar{3}m$ symmetry. Ordering the two $3a$ sites on this lattice leads to the GeTe structure in (b), lowering symmetry to $R3m$, while retaining the same two $3a$ sites.

ous work on $\text{Sb}_{1-x}\text{As}_x$ has found that these elements are miscible across the full composition range.^{13,14} Ohya studied the thermal conductivity of $\text{Sb}_{1-x}\text{As}_x$ and speculated that an anomaly around $x = 0.5$ might arise from an ordered compound but lacked any structural characterization to substantiate this claim.¹⁵

While no pure elements outside Group V can form the A7 structure, the isoelectronic IV-VI compound GeTe is closely related. It is simply an ordered arrangement of the same structure, shown in Figure 1(b), with space group $R3m$ in contrast to $R\bar{3}m$ for A7. GeTe might make a promising ferroelectric were it not for large concentrations of free carriers arising from Ge vacancies and a Fermi energy lying within the valence band.¹⁶⁻¹⁸ Again, the GeTe structure is a consequence of s - p hybridization and lone pairs on both Ge and Te.¹⁹ No other pure com-

pounds are known to crystallize in the GeTe structure, as nearby IV-VI compositions form the GeS or rocksalt structures, which are only small displacements away.²⁰

Distinguishing between GeTe-type chemical ordering ($R3m$) versus an A7 solid solution ($R\bar{3}m$) is very difficult—no new Bragg peaks arise upon lowering symmetry, so careful analysis of high-quality scattering data is required. For that reason, and to make clear the case for chemical ordering, we investigated SbAs using single crystal diffraction, high-resolution synchrotron powder diffraction, and pair distribution function (PDF) refinements. All find preference for 80/20 ordering of Sb and As. The PDFs do not show any short As-As distances which would signal the onset of nanoscale phase separation that is invisible to Bragg diffraction.^{21–24} High-temperature Bragg diffraction finds the atomic mixing to become disordered above 300°C.

Transport and reflectivity measurements confirm that SbAs is a semimetal with band overlap, in agreement with our first-principles calculations. While the Seebeck coefficient and plasma frequency of SbAs lie between those of Sb and As, the optical dielectric constant is found to be outside the end members, implying a widening of the direct band gap below the Fermi energy, indicating complex band structure changes. In the case of BiSb, this band shifting leads to opening of a semiconducting energy gap. None is found so far in SbAs, but the effects of doping and annealing remain a topic of further investigation.

II. METHODS

SbAs single crystals were prepared from elemental Sb (99.99%) and As (99.999%). The powders were loaded into 9 mm-diameter quartz tubes and sealed under vacuum. Tubes were heated at 10°C/min to 800°C, at which point the samples were molten. Samples were held at this temperature for 30 min and periodically flipped to homogenize, then water quenched to avoid an incongruent melting transition.²⁵ Still sealed under vacuum, tubes were placed into a furnace preheated to 630°C to anneal for 60 h, then cooled to room temperature at 10°C/min. Under these conditions SbAs crystallized into shiny, mirror-like crystals about 1 mm per side, typically with triangular facets and easily cleaved into plates along $\{001\}$ planes.

Single crystal X-ray diffraction data were collected up to $\theta = 35.28^\circ$ on a STOE 2T image plate diffractometer equipped with Mo- $K\alpha$ radiation ($\lambda = 0.71073 \text{ \AA}$) at room temperature. Data reduction and integration absorption correction were performed using X-Area software provided by STOE. The crystal structure was solved using direct methods and refined by a least-squares refinement using the SHELXTL suite of programs.²⁶ All atomic displacement parameters were refined anisotropically. A twin law (-1 -1 0 0 1 0 0 0 -1) was applied and refined to 50.2%. The final composition refined to

$\text{Sb}_{0.94}\text{As}_{1.06}$. Crystallographic parameters are given in Table I.

High-resolution synchrotron X-ray powder diffraction was performed at beamline 11-BM of the Advanced Photon Source (APS), using 30 keV x-rays ($\lambda = 0.413284 \text{ \AA}$) and crystals ground and sieved to 45 μm . High-temperature diffraction was performed at beamline 1-BM using 20 keV x-rays ($\lambda = 0.6128 \text{ \AA}$) and samples sealed under vacuum in quartz capillaries. Time-of-flight neutron powder diffraction data were collected at the NPDF instrument at Los Alamos National Laboratory. Rietveld refinement was performed using the EXPGUI frontend²⁷ for GSAS.²⁸ Unit cells and Fourier maps are plotted using VESTA.²⁹

High-momentum-transfer total scattering data were collected at APS beamline 11-ID-B (90 keV, $\lambda = 0.13702 \text{ \AA}$), and the aforementioned NPDF instrument (neutron time-of-flight). Extraction of the PDF was performed using PDFGetX2³⁰ and $Q_{max} = 25 \text{ \AA}^{-1}$ for x-ray data, and PDFGetX3³¹ with $Q_{max} = 35 \text{ \AA}^{-1}$ for neutron data. Least-squares fits to the PDF were conducted with PDFgui.³²

Resistivity measurements were performed in 4-point geometry using a Quantum Design PPMS. The Seebeck coefficient (thermopower) of a polycrystalline SbAs ingot was measured under helium atmosphere using an ULVAC-RIKO ZEM-3 system. Samples used for infrared (IR) reflectivity were annealed at 630°C for 30 h and cooled to room temperature in 60 h, resulting in large ingots. A flat surface of the sample was alumina polished and washed with ethanol. The reflectivity spectrum was recorded as a function of wavenumber, in nearly normal incidence, in the spectral range 100-4000 cm^{-1} with a Nicolet 6700 FTIR spectrometer equipped with a Spectra-Tech spectral reflectometer.

Electronic band structures and densities of states (DOS) were calculated for the hexagonal unit cell of SbAs using density functional theory (DFT). We used a perfectly ordered arrangement of SbAs but allowed for relaxation. All calculations used the projector-augmented wave method^{33,34} and the generalized gradient approximation to exchange correlation, developed by Perdew-Burke-Ernzerhof,³⁵ as implemented in the VASP code.^{36–38} A planewave energy cutoff of 400 eV was used and convergence was assumed when the energy difference between subsequent self-consistent cycles was less than 10^{-4} eV. Self-consistent calculations were done using $12 \times 12 \times 6$ Monkhorst-Pack \mathbf{k} -point sampling³⁹ and the DOS is obtained by using a finer \mathbf{k} -mesh of $18 \times 18 \times 9$. Scalar relativistic effects and spin-orbit interactions were included. Thermopower S calculations using the Boltzmann transport equation and constant relaxation time were performed with the BoltzTrap package written by Madsen and Singh.⁴⁰

TABLE I. Structural parameters obtained from room-temperature single-crystal refinement (full-matrix least-squares on F^2) of SbAs. $R_1 = \Sigma||F_o| - |F_c||/\Sigma|F_o|$, $wR_2 = \{\Sigma[w(|F_o|^2 - |F_c|^2)^2]/\Sigma[w(|F_o|^4)]\}^{1/2}$

Formula	Sb _{0.94} As _{1.06}
Formula Weight	193.86 g/mol
Crystal system	Trigonal
Space group	$R\bar{3}m$
$a = b$	4.0655(7) Å
c	10.889(3) Å
V, Z	155.87(5) Å ³ , 3
ρ	6.196 g/cm ³
Absorption coefficient	28.748 mm ⁻¹
$F(000)$	249
θ_{max}	34.62°
Reflections collected, unique	762, 197
Unique reflections	197
R_{int}	0.0203
Number of parameters	11
Goodness-of-fit on F^2	1.311
Final R indices [$I > 2\theta(I)$]	0.0117 R_1 , 0.0287 wR_2

III. RESULTS AND DISCUSSION

A. Structural refinement

Single-crystal diffraction provides the most observed reflections per refined parameter and so is the preferred method to determine whether SbAs forms an ordered compound or solid solution. The cell parameters and refinement details are summarized in Table I, while the atomic parameters are given in Table II. It must be noted that lowering symmetry from the A7 solid solution space group $R\bar{3}m$ to GeTe-type $R\bar{3}m$ does not result in the appearance of any new reflections. Only the peak *intensities* hold information about chemical ordering. We found that the cell contains two sites with different scattering density. The refinement indicated that an approximate 80/20 occupation of each site (see Table II) significantly improves the fit versus a pure solid solution: refinements with even site mixing in the $R\bar{3}m$ space group gave final R indices of $R_1 = 0.0270$ and $wR_2 = 0.0754$ with a goodness-of-fit on F^2 of 1.527. This implies that SbAs has GeTe-type ordering with $\sim 20\%$ antisite disorder. More complete ordering might be attainable by annealing below the ordering temperature which we discuss subsequently.

Single crystal refinement indicates that SbAs is mostly ordered, but the two structures produce such similar diffraction patterns that multiple probes should be used to confirm correct occupancy. To that end, we performed synchrotron powder diffraction at beamline 11-BM of the APS, which provides unparalleled resolution and signal/noise ratio for powder samples.⁴¹ The 11-BM data

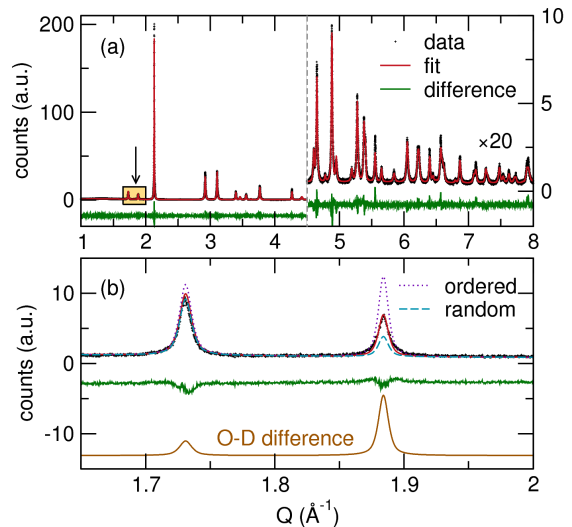


FIG. 2. (Color online) Rietveld refinement of SbAs using synchrotron X-ray radiation at beamline 11-BM of the APS. The full refinement range is given in (a), with the high- Q region enlarged to show detail. Ordering between Sb/As produces a change in intensity in the $\{101\}$ peak at $Q = 1.88$ Å⁻¹, highlighted and arrowed. This area is enlarged in (b), where the experimental and refined pattern is compared to the model using fully-ordered (dotted) and random solid solution (dashed). The difference between the two models (O-D difference) is shown at the bottom of (b). The largest intensity variation in the pattern lies on the $\{101\}$ peak.

is shown in Figure 2 and the Rietveld fit is excellent. The 11-BM refinement comes to the same occupancies and U_{ij} atomic displacement parameters as the single-crystal refinement, within the margins of experimental error (Table II).

Powder diffraction patterns allow us to visualize how much intensity is attributable to chemical ordering: the difference in the diffraction patterns for ordered and solid-solution SbAs models (“order-disorder difference”) is plotted at the bottom of each pane in Figure 2. The difference was within the noise of conventional Cu- $K\alpha$ diffraction data. The region with the largest order-disorder difference is highlighted in Figure 2(a) and magnified in Figure 2(b). Here, the exceptional signal/noise ratio of 11-BM data provides distinction between the ordered (dotted) and disordered (dashed) models in the $\{101\}$ peak at $Q = 1.88$ Å⁻¹. From this view the increased experimental intensity versus the disordered model is clear, providing strong evidence for ordering.

Since the diffraction pattern is the Fourier transform of the scattering potential and the experimental structure factors $|F_{obs}|$ can be extracted directly from the 11-BM data, a Fourier map can be constructed that contains the three-dimensional distribution of scattering density in the cell.

The $\{100\}$ slice of this map is attached to the side of the unit cell in Figure 3 to show the relationship between the Sb and As sites and their location on the map. The

TABLE II. Atomic parameters obtained from single-crystal and synchrotron powder refinement of SbAs. Atomic displacement parameters U_{ij} are given in units of \AA^2 . For powder and PDF refinements, the total occupancy of each site was constrained to be 1, but the antisite fraction was not constrained to be identical for both sites.

Atom	x	y	z	Occupancy	$U_{11} = U_{22}$	U_{33}	U_{12}	$U_{13} = U_{23}$
single-crystal Mo-K α refinement								
Sb(1)	0	0	0	0.74(7)	0.015(1)	0.017(1)	0.008(1)	0
As(1)	0	0	0	0.26(7)	0.015(1)	0.017(1)	0.008(1)	0
As(2)	0	0	0.4623(1)	0.80(9)	0.016(1)	0.017(1)	0.008(1)	0
Sb(2)	0	0	0.4623(1)	0.20(9)	0.016(1)	0.017(1)	0.008(1)	0
powder 11-BM synchrotron refinement								
Sb(1)	0	0	0	0.799(4)	0.0121(3)	0.0163(8)	0.0061(1)	0
As(1)	0	0	0	0.201(4)	0.0121(3)	0.0163(8)	0.0061(1)	0
As(2)	0	0	0.46130(6)	0.783(5)	0.0158(4)	0.019(1)	0.0078(2)	0
Sb(2)	0	0	0.46130(6)	0.217(5)	0.0158(4)	0.019(1)	0.0078(2)	0
X-ray PDF least-squares refinement								
Sb(1)	0	0	0	0.84	0.0138	0.0158	0.007	0
As(1)	0	0	0	0.16	0.0138	0.0158	0.007	0
As(2)	0	0	0.462	0.89	0.0228	0.0197	0.011	0
Sb(2)	0	0	0.462	0.11	0.0228	0.0197	0.011	0

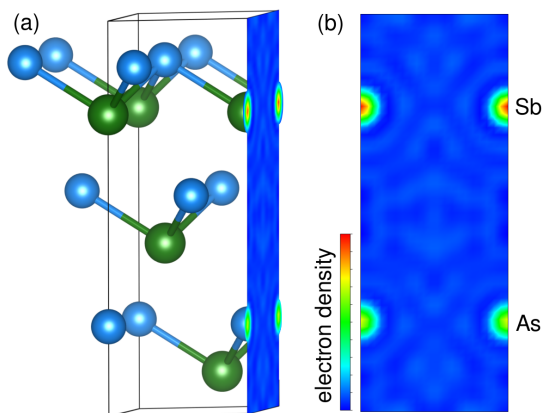


FIG. 3. (Color online) The refined structure (a) from 11-BM X-ray data is shown with a Fourier map of observed structure factors F_{obs} on the $\{100\}$ face. The slice is viewed normal to the plane in (b), with stronger scattering density evident on Sb versus As sites.

$\{100\}$ Fourier map viewed normal to the plane in Figure 3(b). Heavier scattering is evident on the Sb site ($Z = 51$ versus $Z = 33$ for As). In a solid solution these two sites would have equal scattering density.

The presence of nanoscale heterogeneity in SbAs cannot be entirely excluded by single crystal and powder refinements, so we turned to PDF analysis. Local-structure PDF studies of the supposed solid solutions (In,Ga)As, Zn(Se,Te), and (Li,Na)AsSe₂ have shown that materials with single-phase Bragg diffraction patterns can exhibit nanoscale clustering of the end members, evidenced by split nearest-neighbor bond distances in the PDF.^{21–23} Could there be nanoscale clustering of Sb-rich and As-

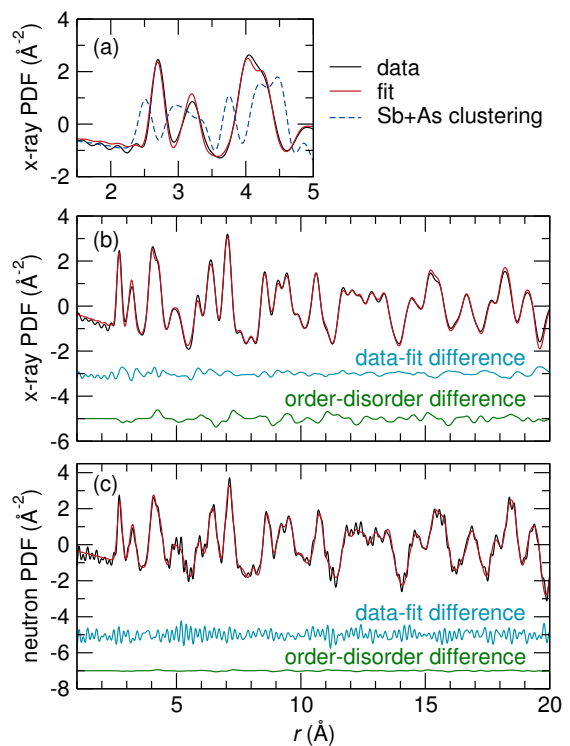


FIG. 4. (Color online) Least-squares refinements to the SbAs PDF collected at room temperature using (a,b) x-rays and (c) neutrons. In both cases, fits are excellent. The inset in (a) shows a two-phase mixture of Sb and As (dashed) that would indicate clustering. This is not present in the data. In the x-ray PDF, the calculated difference between ordered and solid-solution SbAs is larger than the noise. In the neutron case, due to similar scattering lengths, this difference is well below the noise threshold.

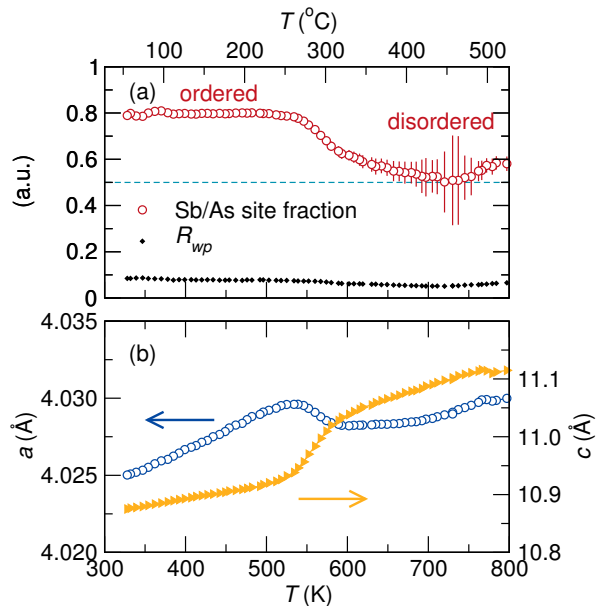


FIG. 5. (Color online) Sequential Rietveld refinements to high-temperature synchrotron x-ray diffraction data (beamline 1-BM, APS) show disordering of Sb/As around 550 K, evidenced by the site occupancy in (a), while maintaining low goodness of fit R_{wp} . In (b), the temperature dependence of the lattice parameters indicates a first-order transition around 550 K.

rich regions, as has been proposed by Levin, et al?⁴² For extensive nanoclustering of Sb and As we would see short bonds corresponding to As–As (2.52 Å), plus long Sb–Sb bonds (2.91 Å). The low- r region of the experimental x-ray PDF in Figure 4(a) shows a fit to the single-phase model from Rietveld refinement, plus a dashed line corresponding to the nanoclustered model. None of the distinct As–As or Sb–Sb bonds are present, eliminating the possibility of extensive nanoscale phase separation.

A unit cell model can be least-squares refined using the PDF, just as was performed using single crystal and powder diffraction data. The x-ray PDF gives the same refined occupancy and atomic parameters as the single-crystal and powder refinements, providing a third check of the Sb/As ordering. The fit is shown in Figure 4(b) and refined values are given in Table II. Neutron scattering does not provide sufficient contrast between Sb and As (5.57 and 6.58 fm scattering cross-sections, respectively) to resolve site ordering in the PDF or Bragg peaks, but higher r -space resolution in the neutron PDF (a result of higher usable Q_{max}) further confirms the absence of nanoscale phase separation by the good fit at low r in Figure 4(c).

High-temperature diffraction data collected upon heating a sample of SbAs at the APS beamline 1-BM refine to the same 80/20 site ordering as other techniques, and results of sequential refinements upon heating are shown in Figure 5. The site occupancy begins to deviate from the room-temperature value around 500 K. A value of

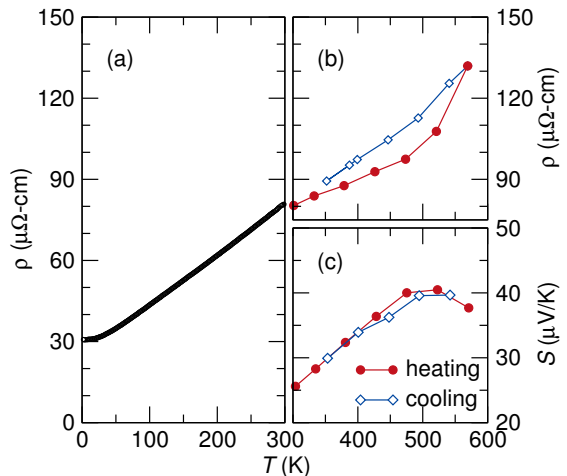


FIG. 6. (Color online) Resistivity (a) of SbAs shows impurity scattering at low temperature and linear temperature dependence, typical of semimetals. Resistivity of an ingot at higher temperatures (b) displays hysteresis, likely due to the phase transition around 550 K. Concurrent measurement of the Seebeck coefficient S (c) shows p -type conductivity with a broad maximum around 500 K.

0.5 in Figure 5(a) corresponds to even mixing (disorder) on both sites, and is marked with a dashed line. Figure 5(b) shows a rapid change in the lattice parameters in the interval $500 \text{ K} < T < 600 \text{ K}$, suggesting a first-order transition around 550 K. Annealing samples below this transition temperature may result in more complete chemical ordering.

B. Transport measurements

Resistivity measurements of SbAs crystals in the ab plane display metallic behavior with $\rho = 80 \mu\Omega\text{-cm}$ at room temperature, shown in Figure 6(a). The large residual resistivity at low T is characteristic of impurity scattering. There is no region where the temperature coefficient of resistivity is negative, as would be expected for a semiconducting region with finite E_g . The behavior of SbAs can be contrasted with the $\text{Bi}_{1-x}\text{Sb}_x$ system, where 7-22% Sb substitution leads to an opening of E_g up to 0.014 eV.^{10,11} Saunders qualitatively suggested that SbAs does not become a semiconductor because the band overlap in As is greater than that in Bi, so a larger perturbation from Sb addition would be required to shift the L -point band enough to create a gap.¹³ Figure 6(b) shows a rise in the resistivity above 500 K, coincident with the order-disorder transition observed by high-temperature diffraction in Figure 5.

The measured thermopower of a polycrystalline SbAs ingot is shown in Figure 6(c). The positive (p -type) behavior and magnitude are similar to that of pure Sb, which reaches a maximum of 30-55 $\mu\text{V/K}$ at 400 K, depending on crystalline orientation.⁴³ The Seebeck coef-

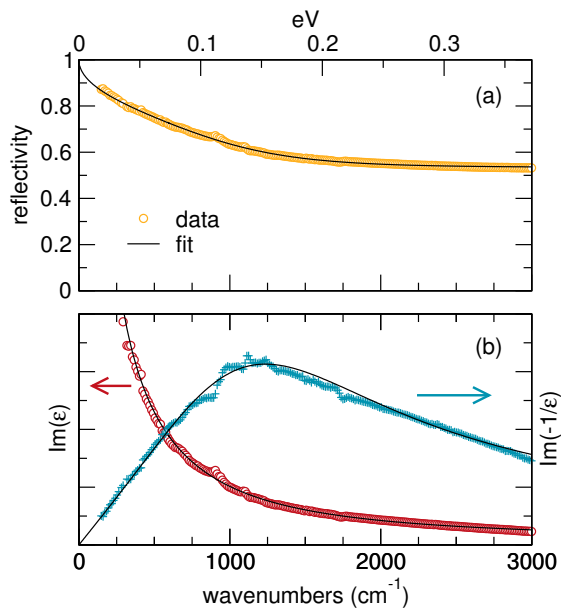


FIG. 7. (Color online) Experimental reflectivity spectrum (a) of SbAs and best-fit calculated reflectivity (solid line) using Equations 2 and 3. The Kramers-Kronig obtained $\text{Im}(\varepsilon)$ and the energy loss function $\text{Im}(-1/\varepsilon)$ are shown in (b). The Drude fit (Equation 3) to $\text{Im}(-1/\varepsilon)$ gives the plasma frequency ω_p and complex dielectric function $\varepsilon(\omega)$.

cient of arsenic is about a factor of 4 smaller.⁴⁴ The decrease in S at high temperatures indicates an increase in n -type character, which could result from the effects of different mobilities for electrons and holes or changes in band overlap due to lattice expansion. Given the intricacies of the band structure near E_F in semimetals, we turn to IR measurements and DFT calculations to understand how chemical ordering in SbAs may affect the band structure.

C. Infrared reflectivity

The experimental reflectivity spectrum of SbAs is shown in Figure 7. This spectrum is dominated by a structureless plasmon, yielding high reflectivity values in the low frequency range with a broad minimum around $\sim 1300 \text{ cm}^{-1}$, followed by almost constant reflectivity values in the high frequency regime. The spectrum was analyzed by the Kramers-Kronig method to obtain the real ε_1 and the imaginary ε_2 parts of the complex dielectric function $\varepsilon(\omega)$. The ε_2 spectrum $\text{Im}(\varepsilon)$ and the energy loss function

$$-\text{Im}(1/\varepsilon) = \varepsilon_2/\varepsilon_1^2 + \varepsilon_2^2 \quad (1)$$

are shown in Figure 7. The $\text{Im}(\varepsilon)$ spectrum is increased in the low frequency range denoting the contribution of free carriers, while the peak in $\text{Im}(-1/\varepsilon)$ indicates a plasma frequency of $\sim 1100 \text{ cm}^{-1}$. The latter represents the fre-

TABLE III. Drude parameters derived from room-temperature reflectivity data of SbAs

$\omega_p \text{ (cm}^{-1}\text{)}$	ε_∞	$\gamma_p \text{ (cm}^{-1}\text{)}$	$\gamma_0 \text{ (cm}^{-1}\text{)}$
1323	41.6	2044	1187

quency of a longitudinal collective mode, when the entire carrier gas system is displaced relative to the fixed ions.

The reflectivity $R(\omega)$ is expressed through the complex dielectric function as

$$R(\omega) = \left(\frac{\sqrt{\varepsilon(\omega)} - 1}{\sqrt{\varepsilon(\omega)} + 1} \right)^2 \quad (2)$$

We find that we can fit the measured reflectivity spectrum of Figure 7(a) with a single-carrier double-damped Drude formula for the complex dielectric function⁴⁵

$$\varepsilon(\omega) = \varepsilon_\infty \left(1 - \frac{\omega_p^2 - i(\gamma_p - \gamma_0)\omega}{\omega(\omega + i\gamma_0)} \right) \quad (3)$$

where ε_∞ is the optical dielectric constant associated with the bound electrons and ω_p is the plasma frequency:

$$\omega_p^2 = \frac{Ne^2}{\varepsilon_0\varepsilon_\infty m^*} \quad (4)$$

where N is the free carrier concentration and m^* is the carrier effective mass. In the typical Drude expression for $\varepsilon(\omega)$, the free carrier damping factor $\gamma_p = 1/\tau$ is considered constant throughout the entire frequency range. In the case of Equation 3, the carrier relaxation time τ is taken to be frequency dependent, giving a frequency dependent damping factor. Here γ_p represents the linewidth of the plasma response centred at $\omega = \omega_p$ and γ_0 represents the linewidth of the absorption at $\omega = 0$. The ratio γ_p/ω_p describes the motion of charge carriers: vibrational when the ratio is small, diffusive or incoherent when the ratio is large. Notice that Equation 3 reduces to the simple Drude expression when $\gamma_p = \gamma_0$.⁴⁶ Fitting the data in Figure 7 gives the parameters in Table III. The single-carrier model fits our data well and also describes the IR reflectivity spectra of $\text{Bi}_{1-x}\text{Sb}_x$ alloys in the semimetallic composition range.^{47,48} This, however, does not exclude a two-carrier system, i.e. electrons and holes, because a two-carrier Drude expression with plasma frequency given by Equation 5 is equivalent to that of a single carrier if the two carriers have the same relaxation time.

$$\omega_p^2 = \frac{e^2}{\varepsilon_0\varepsilon_\infty} \left(\frac{N_e}{m_e^*} + \frac{N_h}{m_h^*} \right) \quad (5)$$

For SbAs the plasma frequency $\omega_p = 1323 \text{ cm}^{-1}$ lies between the two end members: 1000 cm^{-1} for Sb,⁴⁹ and 2419 or 2017 cm^{-1} for two different orientations of As.⁵⁰ Using the values of Table III and Equation 4 we calculated $N/m^* = 8.14 \times 10^{20} \text{ cm}^{-3}$ for SbAs, which also lies

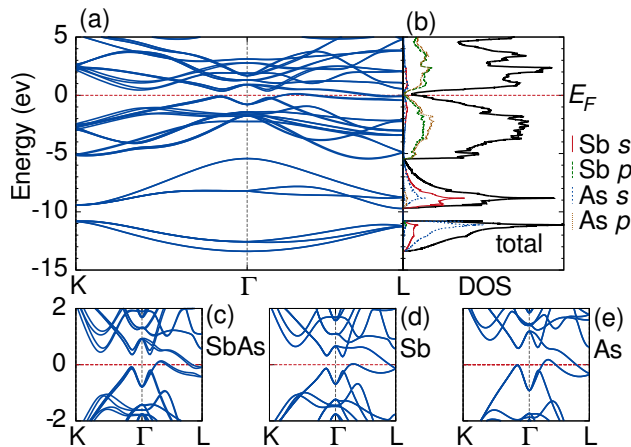


FIG. 8. (Color online) Electronic structure of SbAs (relativistic and spin orbit interaction are included): (a) Band structure with a pseudogap along the ΓL direction; (b) projected density of states (DOS) showing a finite value at E_F . Detailed band structures around E_F are shown below for (c) SbAs, (d) pure Sb, and (e) As.

between the respective values for Sb and As (5.9×10^{20} and $8.9 \times 10^{21} \text{ cm}^{-3}$, respectively).^{49–51}

Meanwhile, the optical dielectric constant ϵ_∞ for SbAs was found to be 41.6, which is less than the values for Sb and As (80 and 50, respectively).^{51,52} The polarizability of the valence electrons relative to both parent materials is decreased, which could be explained by the empirical Moss relation, $\epsilon_\infty \propto E_g^{-1}$, which implies that ϵ_∞ decreases as the direct band gap E_g increases. This relation holds in $\text{Bi}_{1-x}\text{Sb}_x$ alloys across the band-opening composition region.^{47,53} A similar direct gap opening at the L point of SbAs, albeit small and below E_F , is found in our DFT electronic structure calculations of SbAs.

Our IR reflectivity measurements confirm that SbAs displays carrier concentrations typical of Sb and As, with band overlap typical of a semimetal. However, the direct band separation probed by ϵ_∞ seems to have opened wider than that of the end members. We conducted first-principles calculations to visualize how chemical ordering affects the band structure.

D. Electronic structure calculations

The calculated band structure and DOS of SbAs are shown in Figure 8(a,b). Our calculations clearly show that SbAs is a semimetal with a pseudogap, in agreement with resistivity and IR experiments. The detailed band structure along $K\Gamma L$ near the pseudogap is given in the Figure 8(c). The valence band maximum (VBM) and conduction band minimum (CBM) occur at $\sim 0.3\Gamma L$ and $\sim 0.9\Gamma L$ resulting in two electron and two hole pockets. The band structure has an interesting feature near the Γ point where the VBM has a local minimum and the CBM has a local maximum. These bands could produce hole

and electron pockets if the chemical potential is moved, for example by doping.

The projected DOS in Figure 8(b) clearly shows the pseudogap structure with finite DOS at the Fermi level (E_F). From the projected DOS, one can see that there is strong hybridization between Sb and As orbitals. Hybridization of Sb s and As s orbitals gives rise to two bands in the DOS from -13.5 eV to -6.5 eV, separated by a gap of ~ 1 eV. The similar picture also applies to the hybridization between Sb p and As p orbitals. However, the separation between the bands is small, giving rise to an overlap region, forming the pseudogap.

Comparing the band structure of SbAs with those of pure Sb and As (Figures 8(c-e)) reveals common features over a large energy scale, but salient differences appear near the pseudogap region. The splitting of the valence and conduction bands at the L point in SbAs is much larger compared to the pure compounds, which results in a larger direct band separation probed by IR reflectivity. The effect of SOI in SbAs is stronger than those in pure Sb and As due to the lowering of symmetry to non-centrosymmetric $R3m$. Our structural refinements confirm the presence of anti-site disorder in the SbAs samples which we measured transport and reflectivity. Further investigation is required to determine how this disorder affects the pseudogap structure and whether it can be tuned by annealing or doping.

Starting from the DFT electronic band structure we calculated the thermopower S . For the nominally undoped system we find that the thermopower is positive $22 \mu\text{V/K}$, in good agreement with our experimental value of $25 \mu\text{V/K}$. However the calculated S is nearly T -independent in the range $300 \text{ K} < T < 550 \text{ K}$, rising from 22 to $26 \mu\text{V/K}$, whereas the experimental value increases from 25 to $40 \mu\text{V/K}$. The origin of this strong T dependence is not clear. The effect of the structural transition around 550 K on the electronic structure near the Fermi energy and consequent change in the chemical potential μ with temperature and hence S merits further theoretical study.

IV. CONCLUSIONS

We find that the compound SbAs forms as an ordered GeTe-type structure with 80/20 ordering upon cooling from just below the solidus temperature, as confirmed by single-crystal x-ray diffraction, high-resolution synchrotron diffraction, and PDF refinements. The low- r PDF data precludes the possibility of nanoscale phase separation of Sb and As. Transport measurements confirm semimetallic behavior analogous to the end members, with the exception of a direct gap splitting that is suggested by IR reflectivity to be larger than that of Sb or As. First-principles calculations indeed find an opening of the direct gap around the L point due to subtle changes in the p orbital hybridization caused by lower symmetry.

The chemical order-disorder transition is found to be around 550 K by Rietveld refinements to high-temperature synchrotron diffraction data. This raises the possibility that improved ordering may be attained by slow-cooling or annealing below this temperature. The maximum in thermal conductivity observed by Ohyama corresponds to ordered SbAs, so the ability to tune this behavior by control of chemical ordering arises. Furthermore, a reinvestigation of the $\text{Sb}_{1-x}\text{As}_x$ phase space is warranted. The related systems $\text{Bi}_{1-x}\text{Sb}_x$ and $\text{As}_{1-x}\text{P}_x$ may also deserve more detailed study. While a wealth of experimental data finds no miscibility gap in $\text{Bi}_{1-x}\text{Sb}_x$, the behavior of $\text{As}_{1-x}\text{P}_x$ is comparatively unknown—

contradictory reports of the hypothetical compound AsP have been summarized by Karakaya and Thompson.⁵⁴

V. ACKNOWLEDGMENTS

Work at Argonne National Laboratory is supported by UChicago Argonne, a U.S. DOE Office of Science Laboratory, operated under Contract No. DE-AC02-06CH11357. This work utilized NPDF at the Lujan Center at Los Alamos Neutron Science Center, funded by the DOE Office of Basic Energy Sciences and operated by Los Alamos National Security LLC under DOE Contract DE-AC52-06NA25396.

-
- * m-kanatzidis@northwestern.edu
- ¹ D. Seo and R. Hoffmann, *J. Solid State Chem.* **147**, 26 (1999).
 - ² X. Gonze, J. Michenaud, and J. Vigneron, *Phys. Rev. B* **41**, 11827 (1990).
 - ³ C. R. da Silva and R. M. Wentzcovitch, *Comput. Mater. Sci.* **8**, 219 (1997).
 - ⁴ O. Degtyareva, M. I. McMahon, and R. J. Nelmes, *High Pres. Res.* **24**, 319 (2004).
 - ⁵ H. J. Beister, K. Strössner, and K. Syassen, *Phys. Rev. B* **41**, 5535 (1990).
 - ⁶ G. A. Saunders, *Contemp. Phys.* **14**, 149 (1973).
 - ⁷ J.-P. Issi, *Aust. J. Phys.* **32**, 585 (1979).
 - ⁸ T. M. Tritt, *Advances in Thermoelectric Materials I* (Academic Press, 2000).
 - ⁹ M. Z. Hasan and C. L. Kane, *Rev. Mod. Phys.* **82**, 3045 (2010).
 - ¹⁰ A. L. Jain, *Phys. Rev.* **114**, 1518 (1959).
 - ¹¹ A. Ibrahim and D. Thompson, *Mater. Chem. Phys.* **12**, 29 (1985).
 - ¹² B. Predel, in *The Landolt-Börnstein Database*, Vol. 5a, edited by O. Madelung (Springer-Verlag, Berlin/Heidelberg) pp. 1–3.
 - ¹³ G. Saunders, G. Cooper, C. Miziumski, and A. Lawson, *J. Phys. Chem. Solids* **26**, 533 (1965).
 - ¹⁴ M. Ohyama, *J. Phys. Soc. Japan* **21**, 1126 (1966).
 - ¹⁵ M. Ohyama, *J. Phys. Soc. Japan* **23**, 522 (1967).
 - ¹⁶ E. Steigmeier and G. Harbeke, *Solid State Commun.* **8**, 1275 (1970).
 - ¹⁷ S. K. Bahl and K. L. Chopra, *J. Appl. Phys.* **41**, 2196 (1970).
 - ¹⁸ K. M. Rabe and J. D. Joannopoulos, *Phys. Rev. B* **36**, 3319 (1987).
 - ¹⁹ P. Fons, A. V. Kolobov, M. Krbal, J. Tominaga, K. S. Andrikopoulos, S. N. Yannopoulos, G. A. Voyiatzis, and T. Uruga, *Phys. Rev. B* **82**, 155209 (2010).
 - ²⁰ U. V. Waghmare, N. A. Spaldin, H. C. Kandpal, and R. Seshadri, *Phys. Rev. B* **67**, 125111 (2003).
 - ²¹ V. Petkov, I. Jeong, J. S. Chung, M. F. Thorpe, S. Kycia, and S. J. L. Billinge, *Phys. Rev. Lett.* **83**, 4089 (1999).
 - ²² P. F. Peterson, T. Proffen, I.-K. Jeong, S. J. L. Billinge, K.-S. Choi, M. G. Kanatzidis, and P. G. Radaelli, *Phys. Rev. B* **63**, 165211 (2001).
 - ²³ T. K. Bera, J. I. Jang, J. Song, C. D. Malliakas, A. J. Freeman, J. B. Ketterson, and M. G. Kanatzidis, *J. Am. Chem. Soc.* **132**, 3484 (2010).
 - ²⁴ D. P. Shoemaker and R. Seshadri, *Phys. Rev. B* **82**, 214107 (2010).
 - ²⁵ Q. A. Mansuri, *J. Chem. Soc.*, 2107 (1928).
 - ²⁶ G. M. Sheldrick, *Acta Cryst. A* **64**, 112 (2007).
 - ²⁷ B. H. Toby, *J. Appl. Cryst.* **34**, 210 (2001).
 - ²⁸ A. Larson and R. Von Dreele, Los Alamos National Laboratory Report **86**, 748 (2000).
 - ²⁹ K. Momma and F. Izumi, *J. Appl. Cryst.* **41**, 653 (2008).
 - ³⁰ X. Qiu, J. W. Thompson, and S. J. L. Billinge, *J. Appl. Cryst.* **37**, 678 (2004).
 - ³¹ P. F. Peterson, M. Gutmann, T. Proffen, and S. J. L. Billinge, *J. Appl. Cryst.* **33**, 1192 (2000).
 - ³² C. L. Farrow, P. Juhas, J. W. Liu, D. Bryndin, E. S. Bozin, J. Bloch, T. Proffen, and S. J. L. Billinge, *J. Phys. Cond. Mat.* **19**, 335219 (2007).
 - ³³ P. E. Blöchl, *Phys. Rev. B* **50**, 17953 (1994).
 - ³⁴ G. Kresse and D. Joubert, *Phys. Rev. B* **59**, 1758 (1999).
 - ³⁵ J. P. Perdew, K. Burke, and M. Ernzerhof, *Phys. Rev. Lett.* **77**, 3865 (1996).
 - ³⁶ G. Kresse and J. Hafner, *Phys. Rev. B* **47**, 558 (1993).
 - ³⁷ G. Kresse and J. Furthmüller, *Comp. Mater. Sci.* **6**, 15 (1996).
 - ³⁸ G. Kresse and J. Furthmüller, *Phys. Rev. B* **54**, 11169 (1996).
 - ³⁹ H. J. Monkhorst and J. D. Pack, *Phys. Rev. B* **13**, 5188 (1976).
 - ⁴⁰ G. K. Madsen and D. J. Singh, *Comput. Phys. Commun.* **175**, 67 (2006).
 - ⁴¹ J. Wang, B. H. Toby, P. L. Lee, L. Ribaud, S. M. Antao, C. Kurtz, M. Ramanathan, R. B. Von Dreele, and M. A. Beno, *Rev. Sci. Instrum.* **79**, 085105 (2008).
 - ⁴² M. Levin, G. Semenova, T. Sushkova, V. Postnikov, and B. Agapov, *Fiz. Tverd. Tela* **45**, 639 (2003).
 - ⁴³ G. Saunders and Ö. Öktü, *J. Phys. Chem. Solids* **29**, 327 (1968).
 - ⁴⁴ G. Saunders, C. Miziumski, G. Cooper, and A. Lawson, *J. Phys. Chem. Solids* **26**, 1299 (1965).
 - ⁴⁵ F. Gervais, *Mater. Sci. Eng. Rep.* **39**, 29 (2002).
 - ⁴⁶ S. Pessaud, F. Gervais, D. de Sousa, R. Lobo, C. Champoux, P. Marchet, A. Catherinot, J. L. Longuet, and F. Ravel, *J. Phys. Cond. Mat.* **12**, 1517 (2000).

- ⁴⁷ N. Stepanov, *Semiconductors* **38**, 533 (2004).
- ⁴⁸ V. Grabov and N. Stepanov, *Semiconductors* **35**, 149 (2001).
- ⁴⁹ T. J. Fox, R. P. Howson, and D. C. Emmony, *J. Phys. D Appl. Phys.* **7**, 1864 (1974).
- ⁵⁰ H. Riccius, *Phys. Lett. A* **37**, 247 (1971).
- ⁵¹ H. Riccius, *Proc. 9th Int. Conf. Phys. Semiconductors* , 185 (1968).
- ⁵² L. Harris and F. R. Corrigan, *J. Opt. Soc. Am.* **54**, 1437 (1964).
- ⁵³ V. M. Grabov, V. V. Kudachin, A. S. Mal'tsev, and N. P. Stepanov, *Russ. Phys. J.* **33**, 267 (1990).
- ⁵⁴ I. Karakaya and W. Thompson, *J. Phase Equil.* **12**, 343 (1991).